EES Catalysis

PAPER

View Article Online
View Journal | View Issue

Cite this: *EES Catal.*, 2025, 3, 337

Vacancy-engineered bismuth vanadate for photoelectrocatalytic glycerol oxidation with simultaneous hydrogen production†

Haoyue Sun, ‡[a] Rui Tang,‡[a] Lizhuo Wang,[a] Yuhang Liang, [a] Wenjie Yang,[a] Zhisheng Lin,[a] Xingmo Zhang,[a] Kaijuan Chen,[a] Weibin Liang, [a] Shenlong Zhao,[a] Rongkun Zheng *[b] and Jun Huang *[a]

Received 1st October 2024,
Accepted 28th December 2024

DOI: 10.1039/d4ey00211c

rsc.li/eescatalysis

Photoelectrocatalytic (PEC) water splitting offers a sustainable pathway for clean H_2 production, and its integration with biomass valorization further enhances eco-economic efficiency. In this study, a $BiVO_4$ catalyst with an optimized oxygen vacancy (Ov-BVO) concentration was grown on a SnO_2 skeleton, achieving efficient PEC glycerol oxidation to selectively produce dihydroxyacetone (DHA) and H_2 under neutral conditions. By incorporating Ov-BVO with SnO_2, the light-harvesting and photo-induced carrier transfer efficiencies were significantly improved. Ov played a crucial role in selectively absorbing and activating the secondary –OH group of glycerol molecules, as revealed by theoretical and experimental studies. However, excessive Ov induced carrier recombination, underscoring the need for an optimal Ov concentration, which was achieved by tailoring heat treatment conditions. The SnO_2/BVO-400 catalyst demonstrated a trade-off between the prolonged carrier lifetime and efficient reactant adsorption, exhibiting a PEC DHA productivity of 144 mmol m^{-2} h^{-1} with 26.5% selectivity, alongside H_2 generation (1850 mmol m^{-2} h^{-1}). This work lays the groundwork to achieve value-added chemical fabrication through neutral PEC glycerol reforming and the potential scale-up of this sustainable technology.

Broader context

The sustainable photoelectrocatalytic (PEC) conversion of glycerol to dihydroxyacetone (DHA) represents a significant advancement in renewable energy and environmental catalysis. Traditional methods rely on acidic conditions, which are costly and environmentally detrimental. This work addresses these challenges by developing a system that operates efficiently under mild, neutral conditions, offering a more eco-friendly and cost-effective solution. By integrating defect-engineering strategies and optimizing oxygen vacancies (Ov) in the catalyst, this study enhances light-harvesting capabilities and improves reaction efficiency, providing a new pathway for biomass valorization. This advancement not only contributes to sustainable chemical production but also opens up doors for scalable applications in the broader field of biomass conversion technologies. The approach reduces energy consumption and operational barriers, aligning with the global push toward carbon-neutral chemical synthesis. The synergy between PEC systems and defect-engineering strategies paves the way for the development of more efficient solar-driven processes, which have the potential to revolutionize biomass conversion and renewable energy industries, supporting a cleaner and more sustainable future. This work represents a critical step in addressing global environmental challenges and advancing the field of solar-driven catalysis.

Introduction

Glycerol reforming to sustainably generate reusable chemicals and fuels is drawing great attention. As the major by-product of the biodiesel industry, millions of tons of glycerol are produced annually.[1] In contrast, crude or refined glycerol prices are extremely low (USD 0.11 kg^{-1}). However, its derived C_3 or C_2 products are all value-added chemicals, among which dihydroxyacetone (DHA) is the most value-added product (USD 150 kg^{-1}). Meanwhile, research has found that formic acid (FA) is robustly generated as the major by-product since intensive competition exists for activating the glycerol molecules' primary and secondary –OH groups,[2] whilst only activating the secondary –OH can generate DHA. Considering that formic acid can be synthesised by many other methods and its price is also

[a] School of Chemical and Biomolecular Engineering, Sydney Nano Institute, The University of Sydney, NSW 2037, Australia. E-mail: jun.huang@sydney.edu.au
[b] School of Physics, Sydney Nano Institute, The University of Sydney, NSW 2037, Australia. E-mail: rongkun.zheng@sydney.edu.au

† Electronic supplementary information (ESI) available. See DOI: https://doi.org/10.1039/d4ey00211c

‡ These authors contributed equally.

relatively low (USD 1.0 kg^{-1}) compared with DHA,[2] realising the high-selective generation of DHA is greatly and eco-economically significant. Currently, selective glycerol oxidation has been achieved by thermal oxidation and electrocatalytic oxidation with noble metal-based catalysts, which are not cost-effective and cause enormous energy consumption and greenhouse gas emissions.

In this regard, photoelectrocatalytic (PEC) glycerol conversion technologies turn into a promising strategy, allowing solar energy to trigger the reaction under low-bias or even un-bias conditions.[3,4] It has been demonstrated that selective PEC DHA generation can be achieved under strong acid conditions (with a pH of 2).[5,6] However, such a harsh reaction condition significantly limits its practical application because of the difficulty and high cost of handling the corrosion issues induced by the acid electrolytes for constructing stable catalysts and electrolysers and storing photo-refinery products.[7,8] Therefore, developing PEC glycerol refinery technologies that efficiently produce DHA under neutral conditions would lower the cost barriers to practically apply this sustainable technology. Developing catalysts that selectively adsorb and activate the targeted –OH of glycerol is of significant importance to achieve such a goal. For instance, Duan *et al.* recently reported that by modifying TiO_2 with Bi_2O_3, the selective activation of the secondary –OH of glycerol could be enhanced, leading to improved solar-driven DHA selectivity in acid electrolytes.[9] Besides the modification strategy, the defect-engineering approach has also been proven effective in tuning the thermal glycerol refining selectivity.[10] However, it remains unveiled if the product selectivity can also be tuned in solar-driven reactions by simply adjusting the atomic structure of the catalyst, which calls for in-depth investigation.

Besides the reaction, catalyst design is another critical issue that significantly affects PEC oxidation reaction performance. The eventual PEC activity is determined by the light-harvesting and charge carrier transfer performance of anode catalysts, which are sensitively influenced by the defect states in the catalysts.[11] Defects with appropriate concentration could greatly promote the catalyst's reaction activity, whilst excessive defects could compromise the reaction performance.[12,13] In addition, considering the optical response capability, $BiVO_4$ is regarded as one of the most promising anode catalysts, and generally shows a band of 2.4–2.7 eV.[14–17] Recently, Liu *et al.* reported a $BiVO_4$ (BVO)-based photoanode for selective glycerol oxidation.[18] However, as a pristine semiconductor material, the charge transfer performance of BVO is still limited.[19] Besides, the most reported BVO-based photoanode has a bulk structure,[20,21] which also limits the light-harvesting capability of the photoanode material, as the anode material could simply reflect the light. SnO_2, an n-type wide bandgap semiconductor (E_g = 3.5 eV),[22] provides a stable framework for BVO, preventing agglomeration and enhancing durability. It improves visible light absorption with increasing photon utilization.[23] Additionally, the formation of a heterojunction of SnO_2/BVO enhances charge separation and transport through band alignment and efficient electron pathways, boosting PEC performance for glycerol oxidation and H_2 production. Therefore, constructing a rationally engineered photoanode could contribute to a more satisfactory PEC glycerol oxidation performance.

Here, we demonstrated a BVO catalyst with an optimal oxygen vacancy (Ov) concentration for highly selective PEC DHA generation under neutral conditions with simultaneous H_2 production. Systematic studies confirmed that growing the BVO catalysts on a SnO_2 skeleton enhanced the photoanodes' light-harvesting and interfacial charge transfer behaviors, which led to an increased current density. By tuning heat treatment conditions, the effect of the Ov on the carrier surface trapping process is investigated by time-resolved spectroscopy and X-ray photoelectron spectroscopy. Then the concentration of the Ov is precisely tailored to achieve the best reaction activity. Finally, it is confirmed by both experimental and theoretical results that the introduction of the Ov into BVO could play a vital role in the selective adsorption and activation of the secondary –OH in glycerol, which results in significantly improved DHA selectivity and productivity in neutral electrolytes.

Results

Effect of annealing condition control on the structure and morphology of BVO

The SnO_2/BVO-x (x = 300, 400, 500, Air) photoanode was synthesised by a two-step growth approach (Fig. 1a). Firstly, the well-crystalised SnO_2 nanosheet skeleton was grown on the FTO substrate through a facile solvent-thermal method. Then, the BVO precursor was spin-coated onto the skeleton, which was then, respectively, annealed in Ar at 300, 400, and 500 °C and in Air at 500 °C. The morphology of the SnO_2/BVO-x (x = 300, 400, 500, Air) photoanode is recorded using a scanning electron microscope (SEM). As shown in Fig. 1b and Fig. S1 (ESI†), the SnO_2 nanosheet is uniformly grown on the FTO substrate with a thickness of *ca.* 2.1 μm.

Moreover, from the front- and cross-sectional SEM images (Fig. 1c and Fig. S2, ESI†), it could be seen that the BVO nanoparticles are evenly distributed on the surface of the SnO_2 nanosheet. This conclusion could be further illustrated by the high-angle annular dark-field scanning transmission electron microscopy (HAADF-STEM) image of SnO_2/BVO-400, as shown in Fig. 1e. From the corresponding energy disperse spectra mapping images (Fig. 1f–h), the uniform distribution of elements Sn, Bi, and V could be evidenced. However, under different heat treatment conditions, the morphologies and composition of the SnO_2/BVO-x (x = 300, 400, 500, Air) materials show no big change (Fig. S3, ESI†). The XRD patterns of the as-synthesised catalysts are shown in Fig. 1d. With BVO grown on SnO_2, it could be evidenced that besides the XRD pattern of the SnO_2 backbones, the XRD peaks of BVO could also be seen. Also, with the annealing temperature, a mixed-phased BVO (tetragonal/monoclinic phase) could be obtained.[24,25] In addition, the increased annealing temperature could result in an obviously enhanced growth of BVO, as the BVO peak intensity becomes more intense with higher heat treatment temperatures.

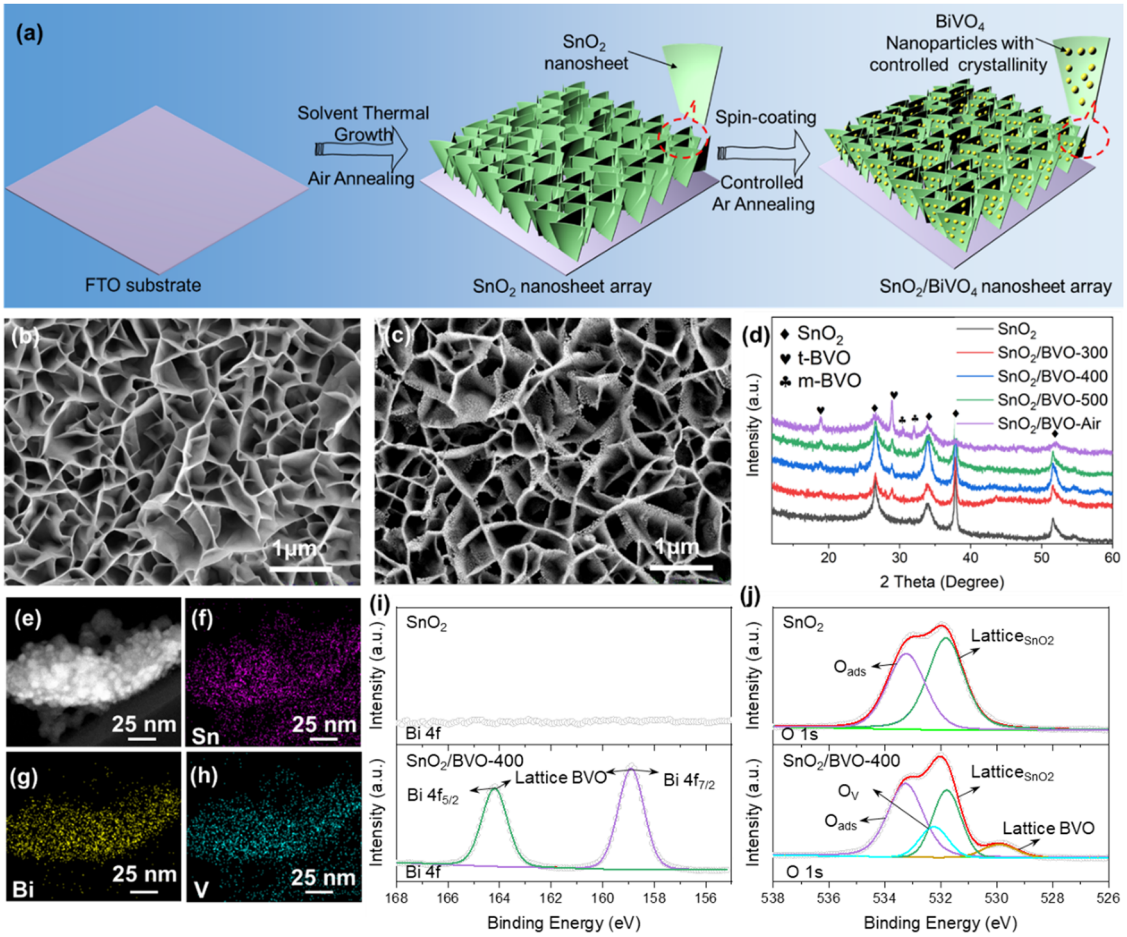

Fig. 1 (a) Schematic synthesis procedure of the SnO_2/BVO nanosheet array photoanode; (b) and (c) SEM images of the pristine SnO_2 nanosheet array and the SnO_2/BVO-400 heterostructure nanosheet array. (d) XRD pattern of pristine SnO_2 and SnO_2/BVO samples under different annealing conditions. (e) HAADF-STEM image of SnO_2/BVO-400, (f)–(h) Sn, Bi, V EDS-mapping images of SnO_2/BVO-400. (i) and (j) High-resolution Bi 4f and O 1s XPS spectra of pristine SnO_2 and SnO_2/BVO-400.

The chemical states of the as-synthesised photoanode catalyst are further investigated through X-ray photoelectron spectroscopy (XPS). The survey XPS spectrum of SnO_2/BVO-400 is shown in Fig. S4a (ESI†), with the elements of Bi, V, Sn, and O being identified. The high-resolution Sn 3d, Bi 4f, and V 2p spectra of SnO_2/BVO-400 show the typical peak shape and positions of SnO_2 and BVO.[26–28] Moreover, the high-resolution Bi 4f and O 1s spectra of SnO_2 and SnO_2/BVO-400 are shown in Fig. 1i and j. Compared to pristine SnO_2, SnO_2/BVO-400 shows obvious Bi 4f peaks and lattice oxygen signals in the Bi 4f and O 1s spectra, confirming the successful loading of $BiVO_4$ on SnO_2, which is in line with the above microscopy results. However, from the O 1s spectrum of SnO_2/BVO-400, it could be noticed that besides the typical oxygen signal from the lattice of SnO_2 and BVO, and the surface adsorbed –OH groups, the signal from the Ov could also be evidenced, which could be induced by the oxygen-deficient heat treatment conditions.[29]

On this basis, to further explore the influence of oxygen-deficient heat treatment on the atomic structure of the catalysts, the HAADF and integrated differential phase contrast (iDPC) images of the SnO_2/BVO-400 are shown in Fig. 2a and b. From the HAADF image, the interface between BVO and SnO_2 could be evidenced. The marked *d*-distance could be attributed to the (121) and (110) facets of BVO and SnO_2, respectively. From the iDPC image, the Ov could be directly evidenced, which is marked in green circles. From the plot intensity profile curve of the framed region in Fig. 2b (as shown in the inset figure of Fig. 2b), the existence of the Ov could be further validated. In this regard, the microscopy results are in line with the XPS results, confirming that Ov defects could be introduced to the lattice of BVO by oxygen-deficient heat treatment.

To gain a deeper understanding of the correlation between heat treatment conditions and the atomic structure of the catalysts, electron paramagnetic resonance (EPR) and XPS analyses were carried out, as shown in Fig. 2c–f and Fig. S5 (ESI†). According to previous work, the Ov-related V^{4+} is paramagnetic, which could be determined by room temperature EPR. As shown in Fig. 2c, it could be seen that, except SnO_2/BVO-Air, all other three samples exhibit strong signals centered at g = 1.977, which matches well with the g value of paramagnetic V^{4+} and confirms the existence of the Ov in BVO.[29] Moreover, regarding the signal intensity, the sample

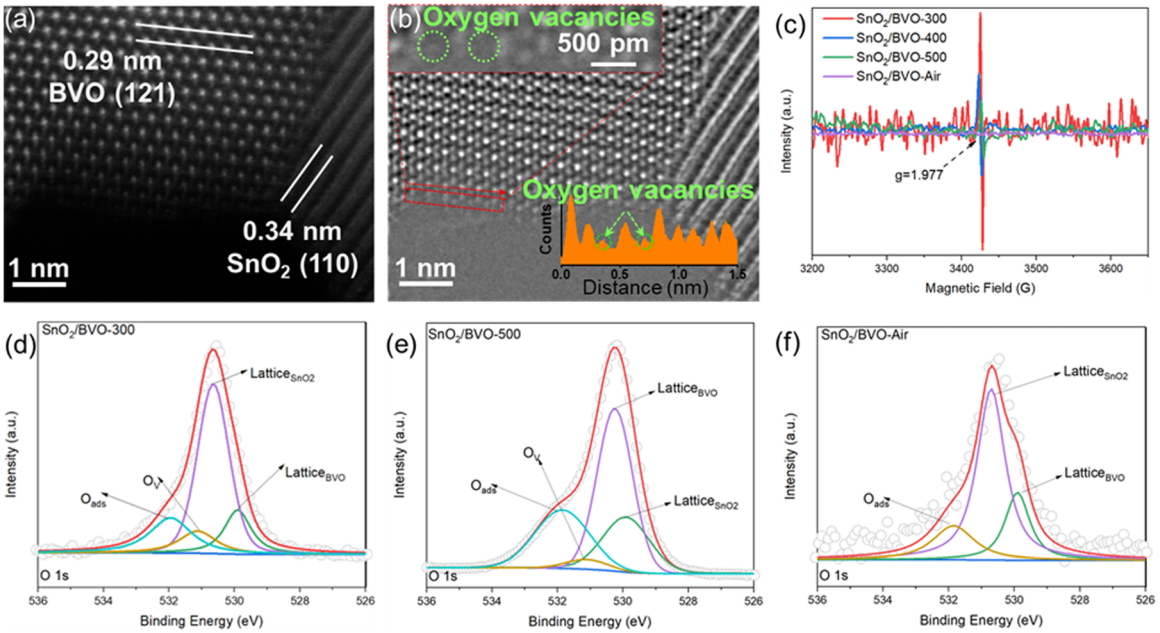

Fig. 2 (a) and (b) HAADF and iDPC images of the SnO_2/BVO-400 sample. (c) EPR spectra of BVO-300, BVO-400, BVO-500, and BVO-Air. (d)–(f) High-resolution O 1s spectra of SnO_2/BVO-300, SnO_2/BVO-500, and SnO_2/BVO-Air.

SnO_2/BVO-300 shows the most intensive signal, indicating the largest amount of Ov. With the increase of annealing temperature, the signal intensity decreased gradually, attributed to the crystallisation of BVO. But for SnO_2/BVO-500, this characteristic signal could still be evidenced, suggesting that the Ov could not be completely diminished in an oxygen-deficient atmosphere, even annealing at high temperatures. Interestingly, for the SnO_2/BVO-Air sample, which is annealed in the Air at 500 °C, it could be seen that the signal disappeared. For this reason, it is believed that higher heating temperature could help the crystal to alter the local structure distortion of BVO, which therefore leads to a decreased Ov concentration.[29]

Through XPS, the chemical states of SnO_2/BVO-x (x = 300, 400, 500, Air) samples are further studied (Fig. 1j and 2d–f). The pristine SnO_2 nanosheet skeleton is well crystallised, as demonstrated by the O 1s XPS peak shown in Fig. 1j. However, for the SnO_2/BVO-x (x = 300, 400, 500) samples (Fig. 2d–f), besides the lattice oxygen from BVO, SnO_2 and surface adsorbed oxygen groups, obvious signals from the Ov could be seen. To better understand the influence of heating temperature on the Ov ratio of BVO, the O 1s spectra of BVO-x (x = 300, 400, 500, Air) are collected and shown in Fig. S6 (ESI†). The Ov/(O_v + O_{BVO} + O_{ads}) ratios of BVO-x (x = 300, 400, 500) samples are calculated to be 24.6%, 20.1%, and 14.7%. This result is in line with the EPR results and confirms that the Ov concentration will decrease with increasing heating temperature.

Energy band structure of defect-engineered catalysts

Ultraviolet-visible (UV-vis) absorption spectroscopy is applied to study the optical response of the obtained photoanode catalysts. Firstly, the absorption spectrum of the SnO_2 nanosheet array as the skeleton is collected (Fig. 3a), which shows quite narrow light harvesting. Combining with the TAUC plot (Fig. S7, ESI†), the band gap of pristine SnO_2 is calculated to be 3.64 eV, which is in accordance with the previously reported work.[30,31] Moreover, it should be pointed out that an enhanced optical response could be evidenced in the range of 400–800 nm. Compared with the absorption spectrum of SnO_2 powder, it could be seen that the SnO_2 nanosheet array shows an enhanced light harvesting performance (Fig. S8a, ESI†). This phenomenon should be attributed to the effective light scattering and trapping process in the array skeleton (as shown in the inset image of Fig. 3a).[32] A similar phenomenon can also be evidenced in the SnO_2/BVO array and powder catalysts (Fig. S8b, ESI†). From the obtained light harvesting curves (shown in Fig. S9, ESI†),[33] the enhanced light harvesting process induced by the array-structured skeleton could also be evidenced, demonstrating the unique morphology advantage of the as-designed photoanode.

Moreover, due to the narrow bandgap of BVO, the SnO_2/BVO-x (x = 300, 400, 500, Air) samples show visible light response capability (Fig. 3a). To understand the effect of the planted Ov on the electronic structure of BVO, the TAUC plots of BVO-x (x = 300, 400, 500, Air) are obtained and shown in Fig. S10a (ESI†). It could be seen that well-crystalised BVO (BVO-Air) shows a bandgap of 2.66 eV. With increasing Ov concentration, the bandgap of BVO decreased slightly. Moreover, according to the valence band XPS(VB-XPS) spectra (Fig. S10b, ESI†), the energy band structure of BVO-x (x = 300, 400, 500, Air) is further calculated. It could be seen that, with increasing annealing temperature, the valence band position gradually increased from 0.99 eV to 1.27 eV for BVO-x (x = 300, 400, 500). Moreover, BVO-Air exhibits a valence band position

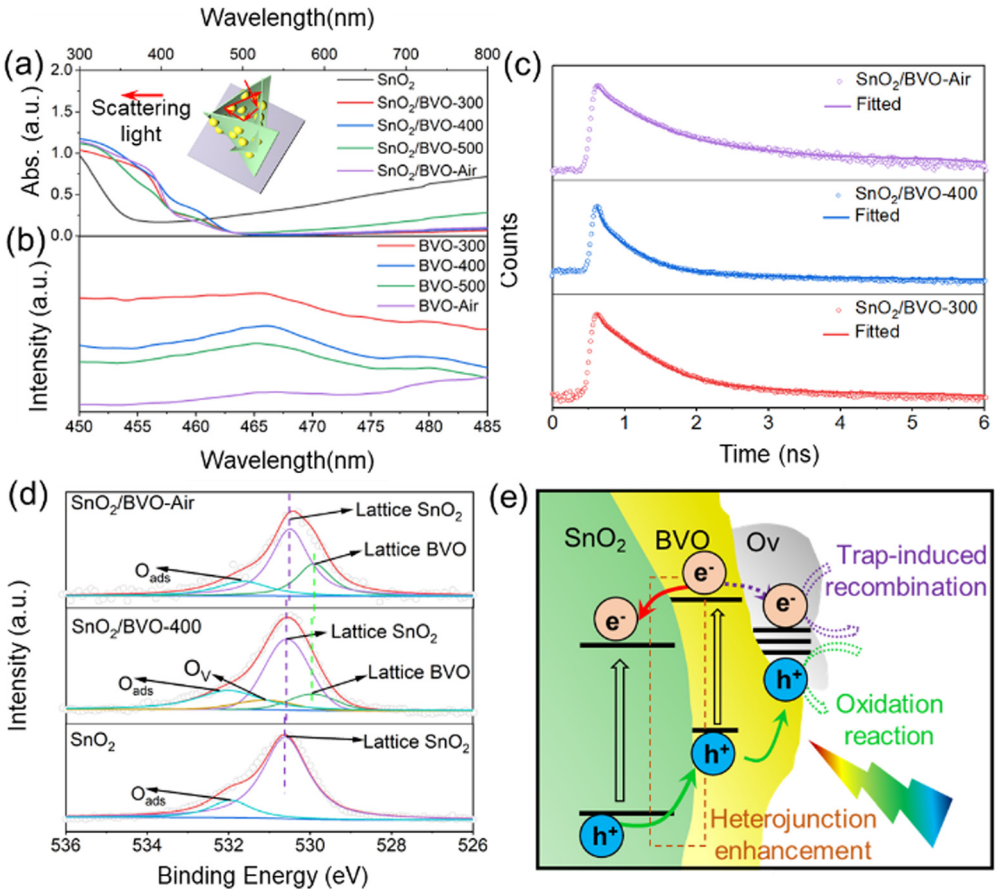

Fig. 3 (a) UV-vis light absorption spectra of SnO_2 and SnO_2/BVO-x (x = 300, 400, 500, Air) samples (with inset showing the light scattering model of the nanosheet array photoanode). (b) Steady-state photoluminescence spectra of BVO-x (x = 300, 400, 500, Air) samples. (c) Time-resolved photoluminescence spectra of SnO_2/BVO-300 and SnO_2/BVO-500 samples. (d) High-resolution O 1s spectra of SnO_2, SnO_2/BVO-400, and SnO_2/BVO-Air. (e) Schematic illustration of the photo-induced carrier transfer process of the SnO_2/BVO photoanode with the Ov in BVO.

of 1.40 eV. These phenomena show that with limited crystallinity and the existence of the Ov, the valence band position of BVO could be uplifted. Consequently, the relative energy band structures of BVO-x (x = 300, 400, 500, Air) are calculated and shown in Fig. S11 (ESI†). By tuning the heat treatment conditions, both the conduction band and valence band position of BVO could shift to low positions with increasing annealing temperature.

Effect on interfacial charge transfer

The effect of heat treatment conditions on the charge transfer behaviours of the photoanode system is further studied, which is of great significance for the PEC reaction. As shown in Fig. 3b, the steady state photoluminescence (SSPL) spectra of BVO-x (x = 300, 400, 500, Air) samples are obtained. It could be seen that all samples exhibit emission peaks at a wavelength of about 460 nm, which is attributed to the charge transfer process between the V 3d and O 2p orbitals in VO_4^{3-}.[34] The BVO-x (x = 300, 400, 500) samples show much higher emission intensity compared with BVO-Air, suggesting that there is better carrier transfer in BVO-Air due to the improved crystallinity. However, due to the limited crystallinity of BVO-300, the excessive Ov could act as the carrier trapping centers and lead to a severe carrier recombination process.

Moreover, the time-resolved photoluminescence (TRPL) spectra of the as-prepared photoanode are obtained and shown in Fig. 3c and Fig. S12 (ESI†). It could be seen that, for all samples, the obtained curve could be fitted by a biexponential decay model. The two decay channels could be explained as the defect-trapping recombination process, for the fast decay component (τ_1), and the charge carrier recombination process between the conduction band and the valence band, for the slow decay component (τ_2).[35] The fitting constants are listed in Table S1 (ESI†). Due to the highest Ov concentration, SnO_2/BVO-300 shows the shortest τ_1 and average carrier lifetime (τ_{ave}). By regulating the heat treatment conditions, τ_1 and τ_{ave} obviously increased in SnO_2/BVO-x (x = 400, 500, Air) samples, indicating that better crystallinity could bring in a better charge transfer process.

To understand the influence of the Ov on the interfacial electron interaction between BVO and SnO_2, the high-resolution O 1s spectra of pristine SnO_2 and SnO_2/BVO-x (x = 400 and Air) are compared and shown in Fig. 3d. For SnO_2 and SnO_2/BVO-Air samples, the negatively shifted SnO_2 lattice O peak of the

SnO_2/BVO-Air sample indicates that there exists an electron transfer process from BVO to SnO_2. This is driven by the thermal dynamic driven force as the conduction band position of BVO is higher than that of SnO_2.[36] However, as for the SnO_2/BVO-400 sample, the above negative shifting trend could still be evidenced, but the intensity is relatively weak. Moreover, precisely observing the O peaks belonging to the lattice of BVO, a contrary positive shift is evidenced for SnO_2/BVO-400. The above results demonstrate that with the existence of the Ov, during the charge transfer process from BVO to SnO_2, some electrons would be captured by the Ov,[37] making fewer electrons reach SnO_2 (shown in Fig. 3e). In this regard, rationally regulating the heat treatment condition is of great significance to realise the appropriate charge transfer process, which is vital for the PEC catalytic reaction.

PEC catalytic performance

As evidenced before, by regulating the heat treatment conditions, the electronic structure and crystal structure could be efficiently regulated. All these factors could directly influence the following PEC performance.

In this regard, the PEC performance was tested under general water-splitting conditions (electrolyte: 0.01 M Na_2SO_4). As shown in Fig. S13 (ESI†), pristine SnO_2 exhibited the lowest current density due to the limited optical response and charge transfer.[38] In comparison, for the SnO_2/BVO-x catalysts, the current densities are obviously enhanced, whilst SnO_2/BVO-400 exhibits the largest current density. Considering the better charger transfer performance exhibited by SnO_2/BVO-500 and SnO_2/BVO-Air, the enhanced PEC activity could come from the better interfacial environment of SnO_2/BVO-400. The Ov could act as the adsorption site for the reaction intermediates and facilitate the surface water oxidation reaction,[39] therefore, a trade-off between the defect-mediated charge transfer and surface reaction could be evidenced from the as-synthesised catalysts. Then, on this basis, the applied bias potential efficiency (ABPE) of the above catalysts is calculated and shown in Fig. S14 (ESI†). SnO_2/BVO-400 exhibits the largest ABPE of 0.21% at a bias of 0.81 V *vs.* RHE, which is much higher than that of other catalysts. It proves that an optimal balance between charge transfer and surface adsorption is of significant importance to the defect-mediated solar energy conversion process.

To explore the glycerol oxidation performance of the designed catalysts, the applied electrolyte was changed to a mixed aqueous solution of 0.01 M Na_2SO_4 and 0.1 M glycerol. It is worth pointing out that, such a low concentration supporting electrolyte (0.01 M Na_2SO_4) is applied to further reduce the

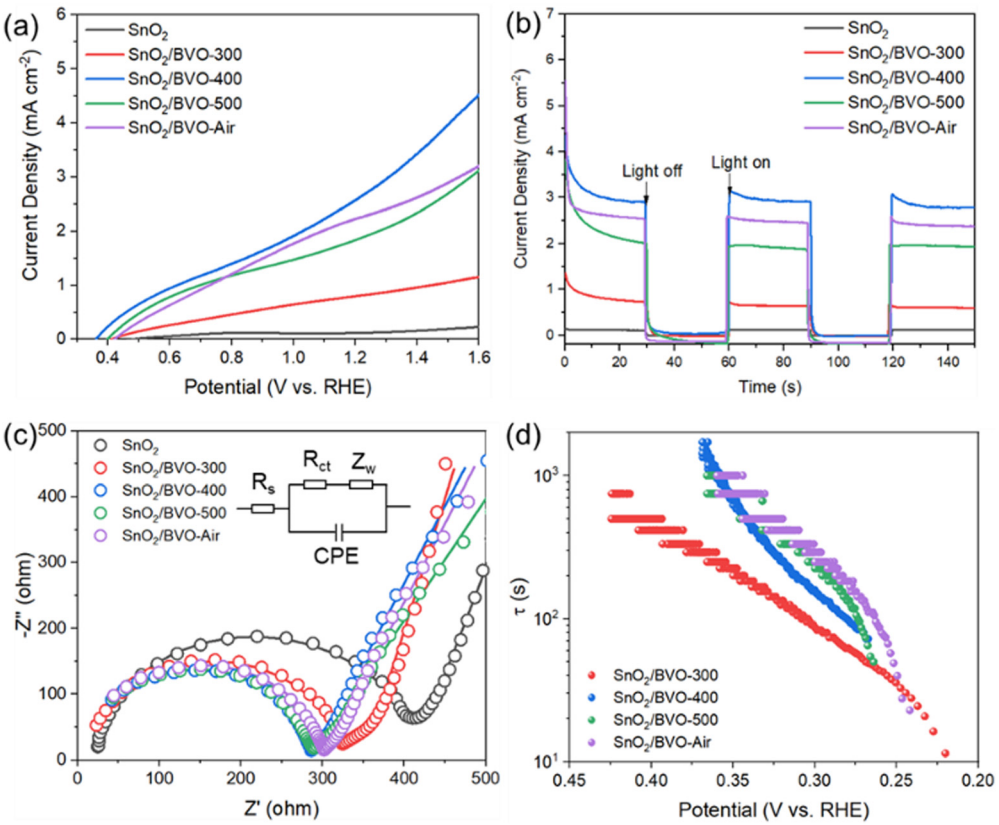

Fig. 4 (a) Linear sweep voltammetry curves of SnO_2 and SnO_2/BVO-x (x = 300, 400, 500, Air) samples in the glycerol electrolyte. (b) The I–t curves of SnO_2 and SnO_2/BVO-x (x = 300, 400, 500, Air) with chopped illumination at a bias of 1.4 V *vs.* RHE. (c) Electrochemical impedance spectra of SnO_2 and SnO_2/BVO-x (x = 300, 400, 500, Air) samples obtained at a bias of 1.4 V *vs.* RHE in the glycerol electrolyte. (d) Average electron lifetime (τ) calculated from the open-circuit potential test of SnO_2/BVO-x (x = 300, 400, 500, Air) samples in the glycerol electrolyte.

raw material costs. All samples showed a similar current changing trend compared to that observed in the PEC water oxidation test (Fig. 4a). The SnO_2/BVO-400 sample still exhibits the largest current density. At a bias of 1.4 V *vs.* RHE, it shows a current density of *ca.* 3.5 mA cm^{-2}. More importantly, SnO_2/BVO-400 also exhibits a larger current density compared with SnO_2/BVO-500 and SnO_2/BVO-Air, which showed better charge transfer. Therefore, the boosted current of SnO_2/BVO-400 could also be attributed to a balance between defect-site induced better reactant adsorption capability and an optimal charge transfer process.

To further illustrate the electrode reaction process, the amperometric *I–t* curves of all samples are recorded under chopped illumination at a bias of 1.4 V *vs.* RHE. As shown in Fig. 4b, all samples show obvious changes during the light on/off cycle, indicating the good optical response of the catalysts. In line with the LSV results, due to the more favourable oxidation kinetics, the catalysts could exhibit larger current density in glycerol oxidation reactions. In addition, it should be pointed out that, the dark current density of the catalyst is relatively small compared to the photocurrent. As a result, the glycerol oxidation reaction is mainly driven by the PEC reaction, rather than the electrocatalytic or photocatalytic reaction (Fig. S15, ESI†). Then the electrochemical impedance spectroscopy (EIS) curves are obtained under the glycerol oxidation conditions as shown in Fig. 4c. The obtained curves are fitted based on the Randles equivalent circuit inserted in Fig. 4c, which contains the solution resistance (R_s), capacitance (CPE), Warburg impedance (Z_w), and the charge carrier transfer resistance (R_{ct}), whilst R_{ct} is represented by the semicircle diameter.[40] According to the fitting constants shown in Table S2 (ESI†), it could be seen that the SnO_2/BVO photoanodes could show an excellent charge transfer capability by constructing heterostructured electrodes.[37] From the details of R_{ct} differences between SnO_2/BVO-*x* (*x* = 300, 400, 500, Air) samples, it could be seen that better crystallinity of BVO can lead to better charge transfer kinetics to the catalysts, as SnO_2/BVO-300 shows a relatively large R_{ct} of 295.2 ohms. However, R_{ct} is influenced by the built-in electric field-induced charge transfer process and the surficial charge injection process since the latter could cause carrier trapping recombination. The efficient glycerol sorption could facilitate surficial carrier consumption and improve charge transfer. Based on the fitting constants, SnO_2/BVO-400 shows the smallest R_{ct}. This should be attributed to an optimal Ov concentration, which results in a balanced defect-mediated charge transfer process.

To further understand the influence of the BVO's atomic structure on the carrier lifetime, the photo-induced carrier lifetime was calculated using the open circuit voltage (OCV) decay plots, which were obtained using the following equation:

$$\tau = \frac{k_B T}{e}\left(\frac{dV_{oc}}{dt}\right)^{-1} \quad (1)$$

where k_B is the Boltzmann constant, e is the charge, and T is the temperature. As shown in Fig. 4d and Fig. S16 (ESI†), compared with SnO_2/BVO-300, the catalysts treated with higher temperatures could exhibit obviously longer carrier lifetime.[41] The largest attenuation rate of SnO_2/BVO-300 comes from the poor crystallinity of BVO, which severely traps the photo-induced carrier. With a reduced Ov ratio, greatly facilitated carrier transfer behaviour is evidenced with simultaneously efficient surficial carrier injection performance. However, upon further increasing the annealing temperature and treating in Air, the existence of the Ov will be minimised and diminished. This will lead to an unfavourable glycerol sorption process, thus further strengthening the carrier recombination in contrast. All the photoelectrochemical results confirm that the trade-off between defect-mediated charge transfer and glycerol adsorption is of significant importance to the reactivity.

The PEC glycerol oxidation products' distribution was further tested and analysed on the SnO_2/BVO-400 sample with different bias potentials. As shown in Fig. 5a, it could be seen that FA and DHA are the main products. It is reported that the solution-based glycerol oxidation[2] leads to generation of a large amount of FA, and because the symmetry molecule possesses two primary –OH groups it could be more easily attacked by the surface adsorbed *OH. In this process, glycerol will be consequently oxidised into GLYD, glyceric acid, and glycolic acid (Fig. 5b). As reported before, GLYD can be easily oxidised into glyceric acid, whilst glyceric acid can be converted to FA *via* C–C cleavage.[9] During the following conversions of glyceric acid to glycolic acid and glycolic acid to formic acid, formic acid will be kept releasing, making FA the primary product.[2] Moreover, since DHA is relatively stable than GLYD, it makes the main by-products are the derivatives of GLYD.[9] With increasing bias, the total product yield rate increased simultaneously, and the most considerable DHA selectivity (26.5%) and yield (144 mmol m^{-2} h^{-1}) are achieved at a bias of 1.4 V *vs.* RHE (Fig. S17, ESI†), whilst a DHA faradaic efficiency of 22% was achieved (Fig. S18, ESI†), which are compatible or even better than those of some latest works (Table S3, ESI†). To date, most research efforts in the field of glycerol reforming have been focused on using strongly acidic electrolytes, which have been found to show the highest selectivity of about 70% for DHA production.[9] However, the acidic environment required for this process leads to significantly increased costs associated with building stable electrolysers and catalysts, as well as the storage of acidic products.[7] While current studies are primarily focused on optimizing catalyst performance under acidic conditions, there is an urgent need for deeper investigation into the development of efficient catalysts for neutral conditions. This study contributes to this effort by presenting a practical approach for selectively reforming glycerol under neutral conditions, which is a promising alternative to the strongly acidic conditions typically used in current research. Although the selectivity for DHA in this study is lower than that achieved under strongly acidic conditions, there is still potential for further improvements (Fig. S19, ESI†). Nonetheless, this work sheds light on a promising avenue for realizing efficiently selective glycerol reforming in a more environmentally benign manner.

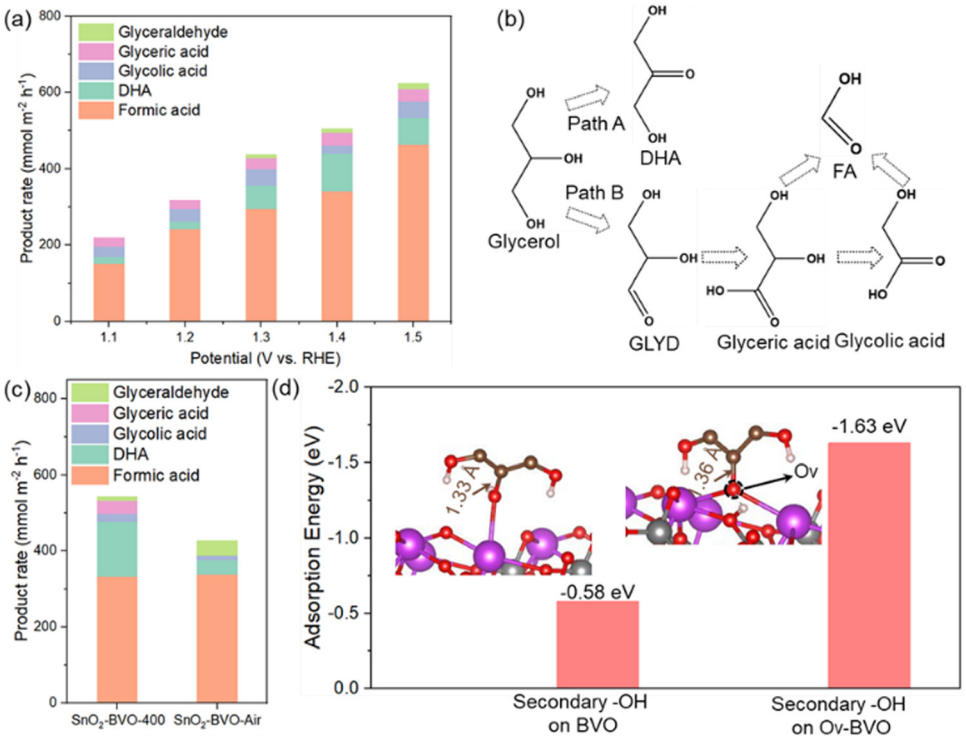

Fig. 5 (a) PEC glycerol oxidation product rate of the SnO_2/BVO-400 photoanode at different bias potentials. (b) Illustration of the typical glycerol oxidation pathway. (c) PEC glycerol oxidation product rates of SnO_2/BVO-400 and SnO_2/BVO-Air at a bias of 1.4 V *vs.* RHE. (d) DFT-optimized structures of the secondary OH^- group adsorbed on general BVO and Ov-BVO.

In addition, after a 3 h reaction, the hydrogen yield rate is about 1850 mmol m^{-2} h^{-1}, which is superior to those of other systems shown in Table S4 (ESI†). In this regard, the electron consumption rate of this process is about 3700 mmol m^{-2} h^{-1}.[42] For the oxidation half-reaction, the hole consumption rate is calculated to be about 3240 mmol m^{-2} h^{-1}. Notably, the electron-to-hole consumption rate was found to be 1.1, indicating a nearly 100% efficiency in terms of producing both DHA and clean hydrogen gas per atom.

To validate the influence of catalysts' fine structure on the catalytic performance, the PEC glycerol oxidation performance of SnO_2/BVO-400 and SnO_2/BVO-Air is investigated at a bias of 1.4 V *vs.* RHE and compared in Fig. 5c. As shown in Fig. 5c, the SnO_2/BVO-Air sample shows much lower DHA selectivity (8%) than SnO_2/BVO-400. To realise the effective glycerol/DHA conversion, besides the surface adsorbed *OH group mediated processes, the selective adsorption and activation of the secondary –OH group of the molecule is of great importance. Therefore, DFT calculation is adopted to clarify further the adsorption and cleavage difference of the secondary OH^- on BVO with different atomic structures (Fig. 5d). It could be seen that with the existence of the Ov, the oxygen atom from the secondary –OH of the glycerol molecules will occupy the Ov position and bond with the two adjacent Bi atoms, with an adsorption energy of −1.63 eV. In comparison, without Ov, the secondary –OH can only link to one Bi atom, with a much smaller adsorption energy of −0.58 eV. Moreover, the stronger secondary C–O bond activation is demonstrated from BVO with the existence of the Ov, with a larger C–O bond elongated from 1.33 Å to 1.36 Å. Moreover, the adsorption energy of the primary –OH on Ov-BVO and the C–O bond length are also calculated and shown in Fig. S20 (ESI†). It could be seen that Ov-BVO shows much larger adsorption energy towards the secondary –OH, which also leads to longer C–O bond length. The Gibbs free energy analysis highlights the catalytic performance differences between BVO and Ov-BVO in the oxidation of glycerol to DHA (Fig. S21, ESI†). BVO, with limited active sites and inefficient charge transfer properties, exhibits higher Gibbs free energy, indicating significant thermodynamic and kinetic limitations. In contrast, Ov-BVO, enhanced by the introduction of oxygen vacancies, demonstrates reduced Gibbs free energy due to the creation of additional active sites and improved charge separation, leading to greater catalytic efficiency. The SnO_2/Ov-BVO surface exhibits the structure of Ov-BVO, especially its oxygen vacancy-driven activity. Therefore, the catalytic behavior of SnO_2/Ov-BVO is very similar to that of Ov-BVO. Considering the enlarged adsorption energy, the significant role of Ov in selective DHA generation can be confirmed. Therefore, it could be concluded that rationally constructed catalysts with precisely designed fine structures are of great importance to realise efficient DHA fabrication with selective secondary –OH adsorption and cleavage behaviour.

To assess the stability of the designed photoanode, long-circular *I–t* curves shown in Fig. S23 (ESI†) indicate no significant current density drop. These results confirm the good stability of SnO_2/BVO-400, suggesting that it is a promising

material for use in photoanodes. The XRD pattern and SEM image were collected for the used SnO_2/BVO-400 and presented in Fig. S24 (ESI†). It shows that the crystallinity of BVO was slightly enhanced, while the nanosheet array appeared thicker after recycling with reduced crystallinity. However, the skeleton structure was well-retained. XPS was utilized to examine the chemical states of Sn, Bi, V, and O in the SnO_2/BVO-400 catalyst after the reaction. The results showed that the oxidation states of Sn (Sn^{4+}), Bi (Bi^{3+}), and V (V^{5+}) remained stable before and after the reaction, indicating the preservation of the catalyst's chemical structure (Fig. S25, ESI†). TEM imaging was conducted to observe any changes in the catalyst's morphology after the reaction. SnO_2 and the BVO retained their structural integrity without noticeable agglomeration or degradation. The interfacial structure between SnO_2 and BVO remained intact, which is crucial for maintaining efficient charge transfer and catalytic activity (Fig. S26 and S27, ESI†). Fig. S28 (ESI†) provides high-resolution iDPC-STEM images illustrating the presence and spatial distribution of oxygen vacancies in the catalyst. The inset at the top of the figure clearly highlights an Ov, indicated by the circled region, showing a distinct contrast difference in the atomic lattice. The corresponding line profile in the lower part of the figure further quantifies this feature, revealing a localized dip in atomic counts at approximately 1.2 nm, consistent with the presence of an Ov. These observations provide compelling evidence for the Ov's existence and its stability within the catalysts' structure.

Conclusion

In this study, a BVO catalyst with an optimal oxygen vacancy (Ov) concentration was grown on a SnO_2 skeleton for efficient PEC glycerol oxidation to produce dihydroxyacetone (DHA) under neutral conditions with simultaneous H_2 production (1850 mmol m^{-2} h^{-1}). It is determined that the SnO_2/BVO type II heterojunction suppressed bulk charge recombination, while the multi-light scattering process enhanced the optical harvesting capability of the catalyst. Meanwhile, the Ov greatly influenced the charge transfer behaviors within BVO, and theoretical calculations and experimental studies demonstrated that the implantation of the Ov played a vital role in the selective adsorption and activation of the secondary –OH group of glycerol molecules in neutral electrolytes, which was crucial for the selective DHA generation. More importantly, the Ov concentration of BVO could be precisely tuned by changing the heat treatment conditions, and an optimal Ov concentration was demonstrated in the SnO_2/BVO-400 catalyst, achieving a trade-off between the photo-induced carrier lifetime and reactants' adsorption. Due to the above synergistic effect, the PEC DHA productivity was 144 mmol m^{-2} h^{-1} with a DHA selectivity of 26.5% under neutral conditions (in a 0.01 M Na_2SO_4 supporting electrolyte), which was almost the best performance compared to those of the other PEC glycerol/DHA conversions reported under neutral conditions. This work provides an example of achieving highly efficient PEC DHA co-generation under non-acid conditions by catalyst engineering, making PEC biomass-to-value added chemical conversion technology closer to practical applications.

Author contributions

Conceptualization, R. T. and H. S.; methodology, H. S. and R. T.; investigation, H. S. and R. T.; experiments, H. S., R. T., L. W., W. Y., Z. L., X. Z., K. C., and W. L.; data storage, R. T., density functional theory calculations, Y. L.; writing – original draft, H. S. and R. T.; writing – review and editing, H. S., S. Z.; R. Z.; and J. H.; funding acquisition, J. H.; and supervision, R. Z. and J. H.

Data availability

The data supporting this article have been included as part of the ESI.†

Conflicts of interest

The authors declare no competing interests.

Acknowledgements

The authors acknowledge the Australian Research Council Future Fellowship (FT220100601), and the Australian Research Council Discovery Project (DP220102851 and DP250104311).

References

1 M. R. Monteiro, C. L. Kugelmeier, R. S. Pinheiro, M. O. Batalha and A. da Silva César, *Renewable Sustainable Energy Rev.*, 2018, **88**, 109–122.
2 Z. Ke, N. Williams, X. Yan, S. Younan, D. He, X. Song, X. Pan, X. Xiao and J. Gu, *J. Mater. Chem. A*, 2021, **9**, 19975–19983.
3 X. Lu, S. Xie, H. Yang, Y. Tong and H. Ji, *Chem. Soc. Rev.*, 2014, **43**, 7581–7593.
4 R. Tang, L. Wang, Z. Zhang, W. Yang, H. Xu, A. Kheradmand, Y. Jiang, R. Zheng and J. Huang, *Appl. Catal., B*, 2021, **296**, 120382.
5 J. Liu, X. Chen, K. Chen, W. Tian, Y. Sheng, B. She, Y. Jiang, D. Zhang, Y. Liu, J. Qi, K. Chen, Y. Ma, Z. Qiu, C. Wang, Y. Yin, S. Zhao, J. Leng, S. Jin, W. Zhao, Y. Qin, Y. Su, X. Li, X. Li, Y. Zhou, F. Ling, A. Mei and H. Han, *Science*, 2024, **383**, 1198–1204.
6 Y. Liu, B. Zhang and D. Yan, *Green Chem.*, 2024, **26**, 2505–2524.
7 Y. Shao, X. Xiao, Y.-P. Zhu and T.-Y. Ma, *Angew. Chem.*, 2019, **58**, 14599–14604.
8 S. Zhao, Y. Wang, Y. Hao, L. Yin, C. H. Kuo, H. Y. Chen, L. Li and S. Peng, *Adv. Mater.*, 2024, **36**, 2308925.
9 L. Luo, W. Chen, S.-M. Xu, J. Yang, M. Li, H. Zhou, M. Xu, M. Shao, X. Kong, Z. Li and H. Duan, *J. Am. Chem. Soc.*, 2022, **144**, 7720–7730.

10 Y. Pan, G. Wu, Y. He, J. Feng and D. Li, *J. Catal.*, 2019, **369**, 222–232.
11 R. Tang, S. Zhou, Z. Zhang, R. Zheng and J. Huang, *Adv. Mater.*, 2021, **33**, 2005389.
12 Y. Wang, J. Zhang, M. S. Balogun, Y. Tong and Y. Huang, *Mater. Today Sustainability*, 2022, **18**, 100118.
13 H. Sun, S. Lee, R. Tang, L. Wang, C. J. Yang, W. Liang, S. Zhao, C. L. Dong, A. Soon and J. Huang, *Adv. Funct. Mater.*, 2024, **34**, 2415859.
14 J. K. Cooper, S. Gul, F. M. Toma, L. Chen, Y.-S. Liu, J. Guo, J. W. Ager, J. Yano and I. D. Sharp, *J. Phys. Chem. C*, 2015, **119**, 2969–2974.
15 J. Wiktor, F. Ambrosio and A. Pasquarello, *ACS Energy Lett.*, 2018, **3**, 1693–1697.
16 Y. W. Lee, P. Boonmongkolras, E. J. Son, J. Kim, S. H. Lee, S. K. Kuk, J. W. Ko, B. Shin and C. B. Park, *Nat. Commun.*, 2018, **9**, 4208.
17 A. Duan, X. Hou, M. Yang, H. Yu, Y. Yang, Q. Ma and X. Dong, *Mater. Lett.*, 2022, **311**, 131498.
18 D. Liu, J.-C. Liu, W. Cai, J. Ma, H. B. Yang, H. Xiao, J. Li, Y. Xiong, Y. Huang and B. Liu, *Nat. Commun.*, 2019, **10**, 1779.
19 R.-T. Gao, X. Liu, X. Zhang and L. Wang, *Nano Energy*, 2021, **89**, 106360.
20 T.-G. Vo, C.-C. Kao, J.-L. Kuo, C.-C. Chiu and C.-Y. Chiang, *Appl. Catal., B*, 2020, **278**, 119303.
21 H. Lu, V. Andrei, K. J. Jenkinson, A. Regoutz, N. Li, C. E. Creissen, A. E. H. Wheatley, H. Hao, E. Reisner, D. S. Wright and S. D. Pike, *Adv. Mater.*, 2018, **30**, 1804033.
22 L. Geronimo, C. G. Ferreira, V. Gacha, D. Raptis, J. Martorell and C. Ros, *ACS Appl. Energy Mater.*, 2024, **7**, 1792–1801.
23 Y. Huo, P. Zhang, J. Chi, F. Fang, Y. Song and D. Sun, *Adv. Energy Mater.*, 2024, **14**, 2304282.
24 A. Zhang, J. Zhang, N. Cui, X. Tie, Y. An and L. Li, *J. Mol. Catal. A: Chem.*, 2009, **304**, 28–32.
25 W. Ma, Z. Li and W. Liu, *Ceram. Int.*, 2015, **41**, 4340–4347.
26 S. Liu, S. Gao, Z. Wang, T. Fei and T. Zhang, *Sens. Actuators, B*, 2019, **290**, 493–502.
27 Y. Liu, X. Li, Y. Wang, X. Li, P. Cheng, Y. Zhao, F. Dang and Y. Zhang, *Sens. Actuators, B*, 2020, **319**, 128299.
28 R.-T. Gao and L. Wang, *Angew. Chem.*, 2020, **59**, 23094–23099.
29 H. L. Tan, A. Suyanto, A. T. D. Denko, W. H. Saputera, R. Amal, F. E. Osterloh and Y. H. Ng, *Part. Part. Syst. Charact.*, 2017, **34**, 1600290.
30 G. Pang, S. Chen, Y. Koltypin, A. Zaban, S. Feng and A. Gedanken, *Nano Lett.*, 2001, **1**, 723–726.
31 G. Yang, C. Chen, F. Yao, Z. Chen, Q. Zhang, X. Zheng, J. Ma, H. Lei, P. Qin, L. Xiong, W. Ke, G. Li, Y. Yan and G. Fang, *Adv. Mater.*, 2018, **30**, 1706023.
32 L. Xu, J. Xu, H. Hu, C. Cui, Z. Ding, Y. Yan, P. Lin and P. Wang, *J. Alloys Compd.*, 2019, **776**, 1002–1008.
33 F. Wu, Y. Yu, H. Yang, L. N. German, Z. Li, J. Chen, W. Yang, L. Huang, W. Shi, L. Wang and X. Wang, *Adv. Mater.*, 2017, **29**, 1701432.
34 R. Bajaj, M. Sharma and D. Bahadur, *Dalton Trans.*, 2013, **42**, 6736–6744.
35 Y. Xiao, C. Feng, J. Fu, F. Wang, C. Li, V. F. Kunzelmann, C.-M. Jiang, M. Nakabayashi, N. Shibata, I. D. Sharp, K. Domen and Y. Li, *Nat. Catal.*, 2020, **3**, 932–940.
36 L. Zhou, C. Zhao, B. Giri, P. Allen, X. Xu, H. Joshi, Y. Fan, L. V. Titova and P. M. Rao, *Nano Lett.*, 2016, **16**, 3463–3474.
37 F. Ning, M. Shao, S. Xu, Y. Fu, R. Zhang, M. Wei, D. G. Evans and X. Duan, *Energy Environ. Sci.*, 2016, **9**, 2633–2643.
38 Z. Zhang, C. Gao, Z. Wu, W. Han, Y. Wang, W. Fu, X. Li and E. Xie, *Nano Energy*, 2016, **19**, 318–327.
39 X. Lv, L. Tao, M. Cao, X. Xiao, M. Wang and Y. Shen, *Nano Energy*, 2018, **44**, 411–418.
40 J. Shan, W. Gao, X. Liu, J. Feng, L. Dai, H. Wang, D. Fan, H. Ma and Q. Wei, *ChemPhysMater*, 2022, **2**(1), 69–96.
41 H. Li, S. Wang, M. Wang, Y. Gao, J. Tang, S. Zhao, H. Chi, P. Zhang, J. Qu, F. Fan and C. Li, *Angew. Chem.*, 2022, **61**, e202204272.
42 Y. Jiang, H.-Y. Chen, J.-Y. Li, J.-F. Liao, H.-H. Zhang, X.-D. Wang and D.-B. Kuang, *Adv. Funct. Mater.*, 2020, **30**, 2004293.